nature geoscience

SUPPLEMENTARY INFORMATION

https://doi.org/10.1038/s41561-019-0434-3

In the format provided by the authors and unedited.

Unique Neoproterozoic carbon isotope excursions sustained by coupled evaporite dissolution and pyrite burial

Graham A. Shields[1*], Benjamin J. W. Mills[2*], Maoyan Zhu[3,4*], Timothy D. Raub[5], Stuart J. Daines[6] and Timothy M. Lenton[6]

[1]Department of Earth Sciences, University College London, London, UK. [2]School of Earth and Environment, University of Leeds, Leeds, UK. [3]State Key Laboratory of Palaeobiology and Stratigraphy & Center for Excellence in Life and Paleoenvironment, Nanjing Institute of Geology and Palaeontology, Chinese Academy of Sciences, Nanjing, China. [4]College of Earth and Planetary Sciences, University of Chinese Academy of Sciences, Beijing, China. [5]School of Earth and Environmental Sciences, University of St Andrews, St Andrews, UK. [6]Global Systems Institute, University of Exeter, Exeter, UK. *e-mail: g.shields@ucl.ac.uk; b.mills@leeds.ac.uk; myzhu@nigpas.ac.cn

Supplementary information 1: Long-term carbon and sulfur cycles

Figure S1 expands on Figure 1 from the manuscript by adding a reconstruction of ocean sulfate concentration (Algeo et al., 2015) and a recent compilation of sulfate $\delta^{34}S$ values (Crockford et al., 2019). Ocean sulfate concentration is estimated to be <8 mM during the late Ediacaran, and seawater $\delta^{34}S$ is estimated to range between around 15 and 40‰.

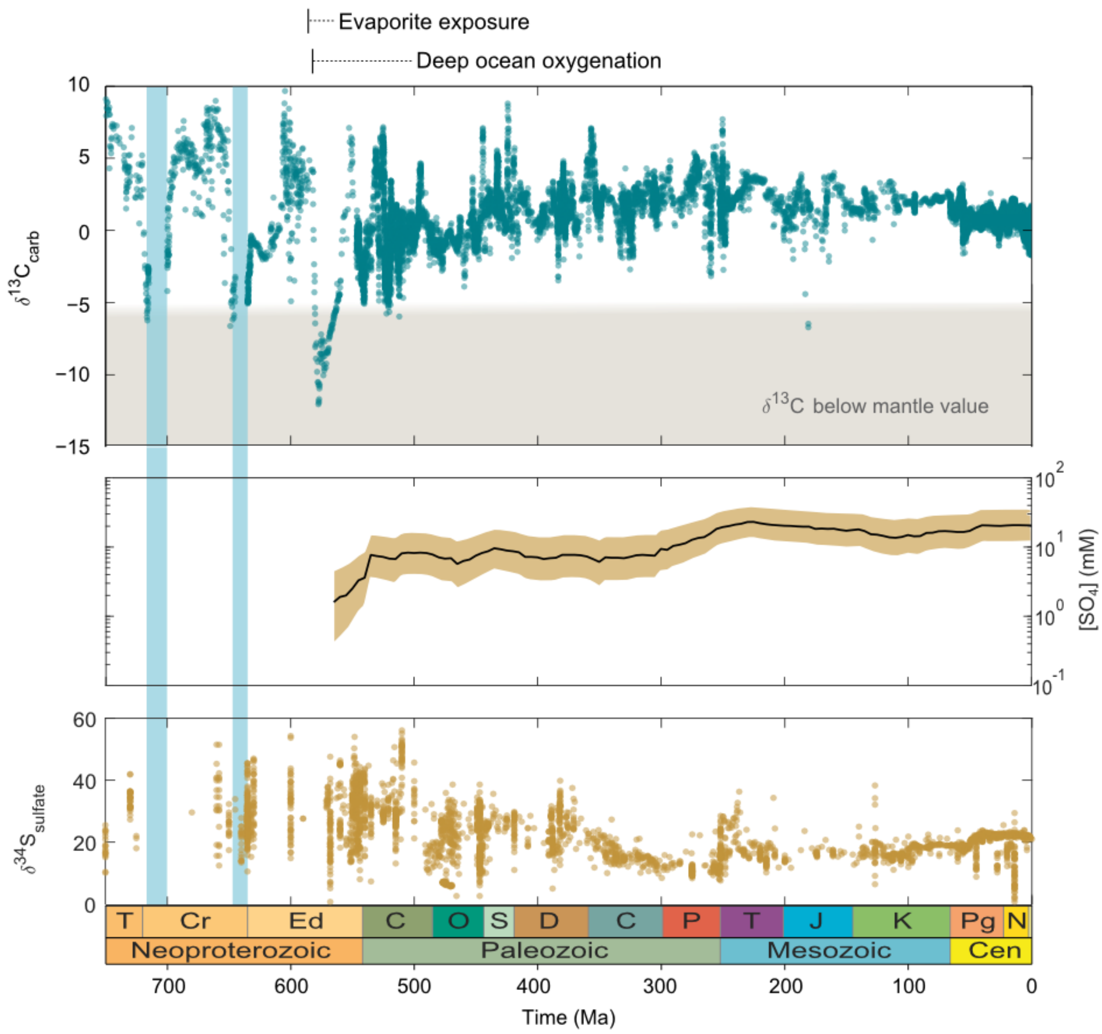

Figure S1. Carbon and sulfur isotopes, and ocean sulfate from late Neoproterozoic to present, *after compilations of Saltzman and Thomas (2012), Crockford et al. (2019) and Algeo et al. (2015).*

Supplementary information 2 additional model runs.

The manuscript introduces a mechanism whereby dissolution of large quantities of evaporite supply marine sulfate, which in turn is buried as pyrite, creating a large long-term O_2 source, and oxidising a marine pool of dissolved organic carbon (DOC). In the model explored in the manuscript, uplift drives weathering of both gypsum and pyrite sulfur, and these fluxes are also assumed to be dependent on global runoff rates. We show simplified simulations in this section which remove the climate-dependence of sulfur weathering fluxes (Figure S2) and also remove the uplift-driven weathering of pyrite (Figure S3). We also run the model for different values of the 'set point' at which oxygen penetrates to the deep ocean and can oxidise the DOC pool (Figure S4), and for different values of the C:P ratio of dissolved organic matter, and potential to supply phosphate to the ocean (Figure S5).

Under all of these modifications, the model outputs for $\delta^{13}C$, and for the global inventories of sulfate, carbon and oxygen are similar to those shown in the manuscript. Thus the mechanism we propose for driving negative carbon isotope excursions is not dependent on modelled climate feedbacks, on uplift-driven weathering of pyrite, or on the potential for P to be released via DOM oxidation. Model predictions for ocean oxygenation occurring after the negative carbon isotope excursion are in line with geological evidence for the late Ediacaran Shuram excursion (Chen et al., 2015). Increases in sulfate concentration between the late Neoproterozoic and early Phanerozoic are also broadly consistent with other inferences (Canfield and Farquhar, 2009), as is the prediction of high CO_2, warm global temperatures and lack of widespread or prolonged glaciation.

The model $\delta^{34}S$ record is strongly dependent on the assumed weathering rates for pyrite. Model $\delta^{34}S$ shows a similar negative excursion to $\delta^{13}C$ when pyrite weathering is included, but less so when it is not. This is because pyrite weathering introduces sulfate with low $\delta^{34}S$ values. Available sulfur isotope data point to a neutral-to-negative $\delta^{34}S$ trend across the Shuram excursion (Fike et al., 2006; Wu et al., 2015), which is broadly consistent with our model, but COPSE includes only a simplified sulfur cycle (e.g. without explicit production and oxidation of H_2S) and further work is needed to uncover the finer details of the sulfur isotope record during negative carbon isotope anomalies.

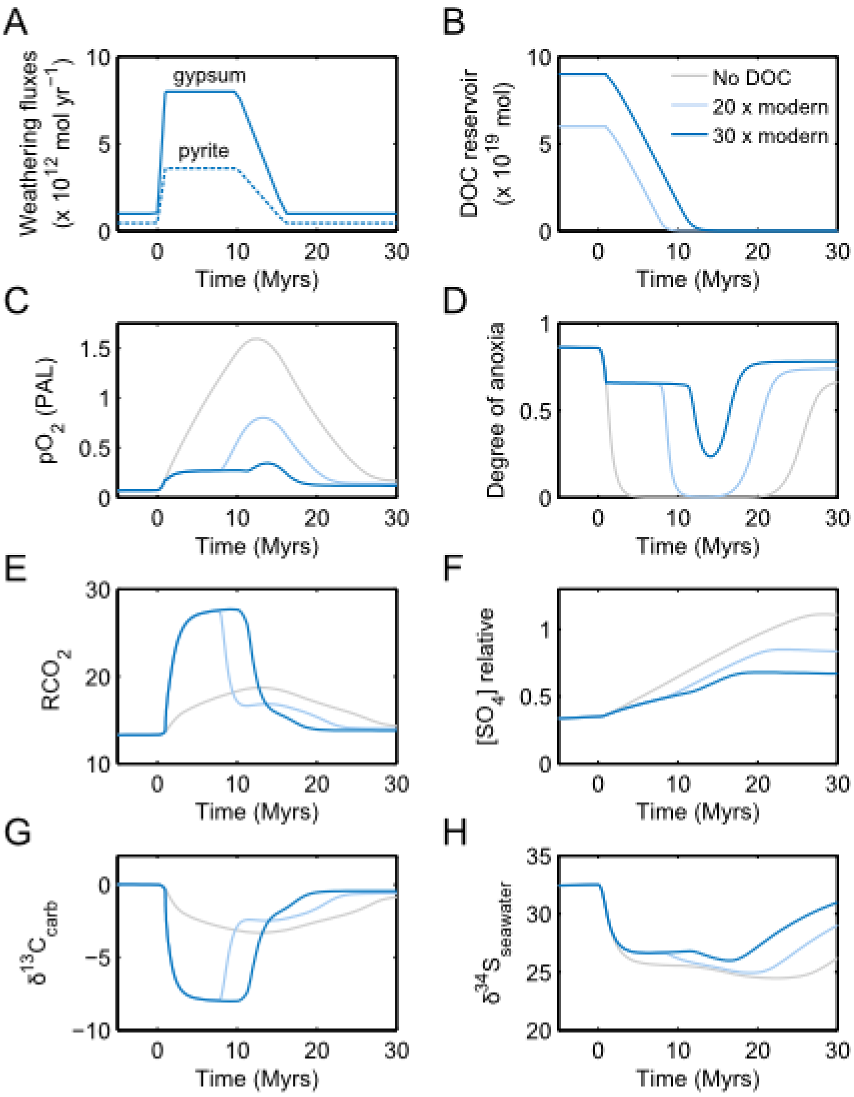

Figure S2. COPSE model run with no climate feedback on sulfate weathering. *A. Input rates of sulphate from pulses of gypsum and pyrite weathering. B. Size of DOC reservoir in moles of carbon. C. Relative atmospheric oxygen concentration. D. Degree of ocean anoxia. E. Relative atmospheric carbon dioxide concentration. F. Relative ocean sulfate concentration. G. Calculated* $\delta^{13}C$ *of new carbonate. H. Calculated seawater* $\delta^{34}S$.

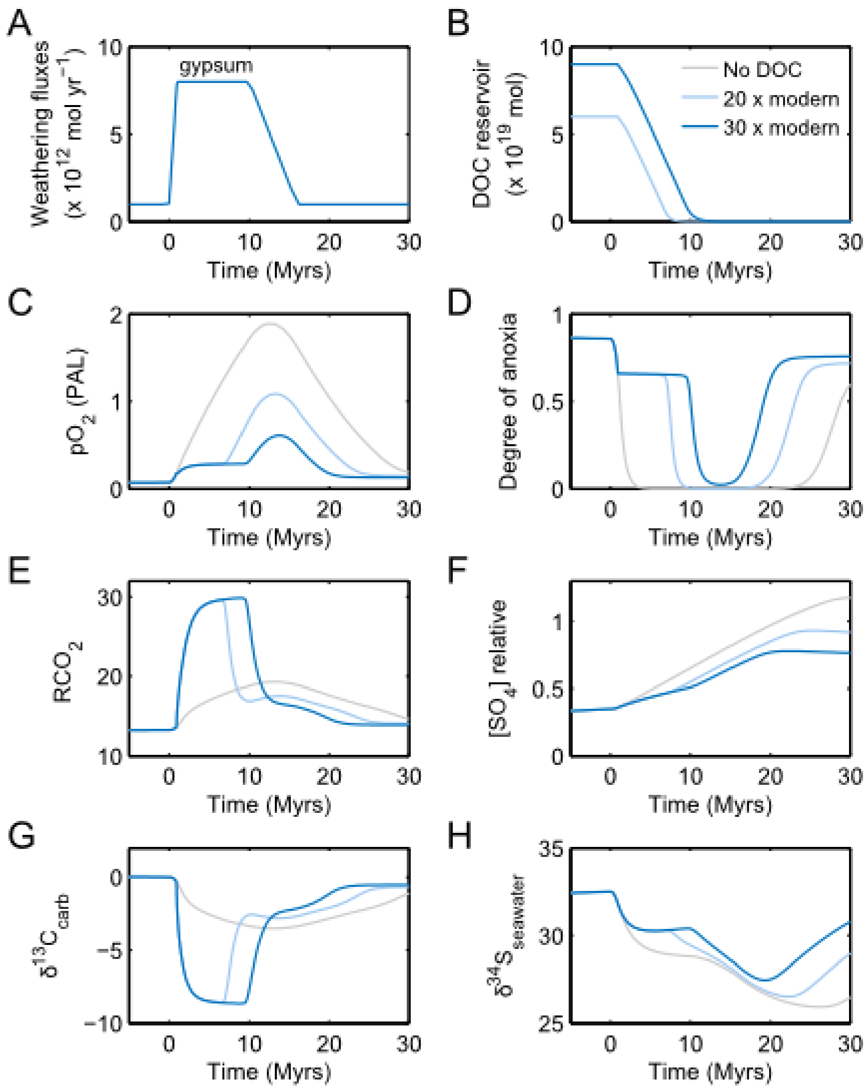

Figure S3. COPSE model run with no climate feedback on sulfate weathering and no pulsed input of pyrite-derived S. *A. Input rates of sulphate from pulses of gypsum and pyrite weathering. B. Size of DOC reservoir in moles of carbon. C. Relative atmospheric oxygen concentration. D. Degree of ocean anoxia. E. Relative atmospheric carbon dioxide concentration. F. Relative ocean sulfate concentration. G. Calculated $\delta^{13}C$ of new carbonate. H. Calculated seawater $\delta^{34}S$.*

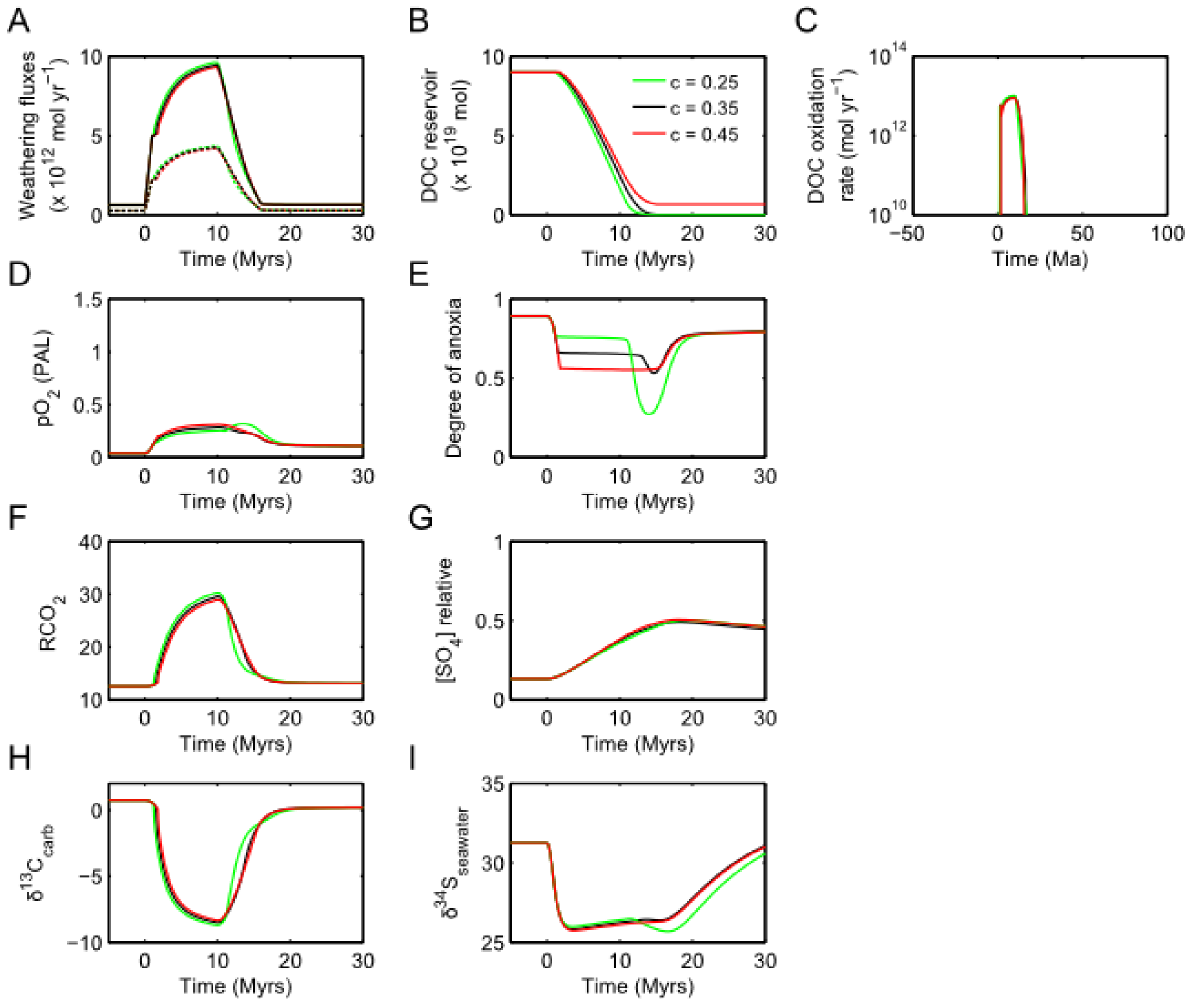

Figure S4. COPSE model run with different set points for DOC oxidation (c in the DOCox equation).

A. Input rates of sulphate from pulses of gypsum and pyrite weathering. B. Size of DOC reservoir in moles of carbon. C. DOC oxidation rate. D. Relative atmospheric oxygen concentration. E. Degree of ocean anoxia. F. Relative atmospheric carbon dioxide concentration. G. Relative ocean sulfate concentration. H. Calculated $\delta^{13}C$ *of new carbonate. I.*

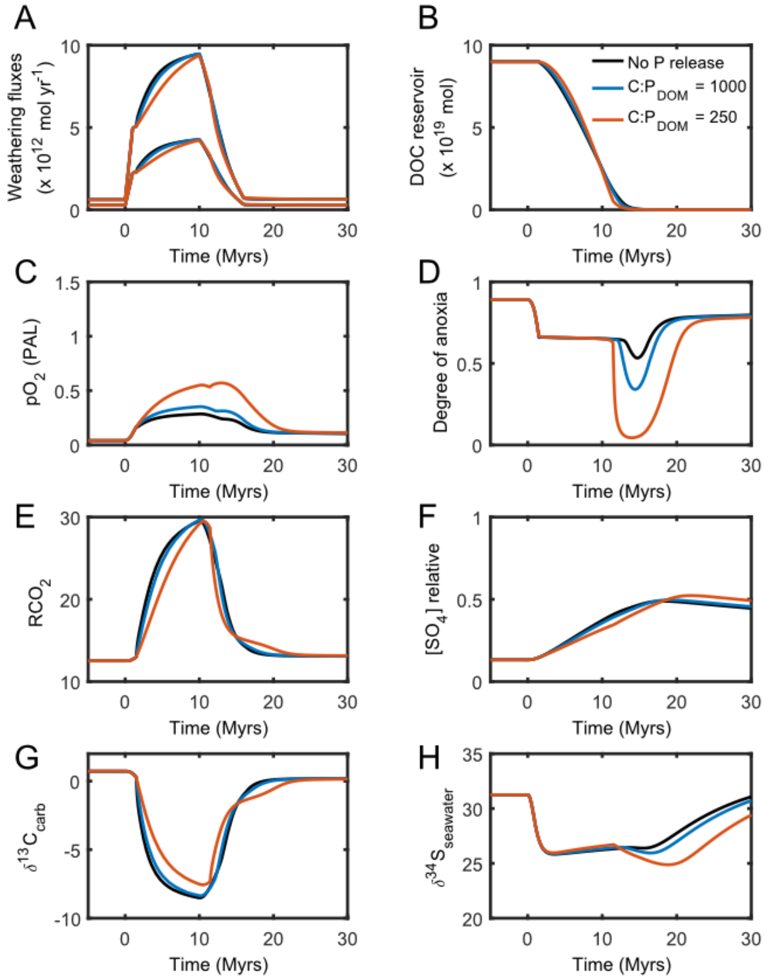

Figure S5. COPSE model run with consideration of potential P release from DOM oxidation. *Consideration of total P release from DOM oxidation makes very little (<1‰) difference to predicted $\delta^{13}C$. A. Input rates of sulphate from pulses of gypsum and pyrite weathering. B. Size of DOC reservoir in moles of carbon. C. Relative atmospheric oxygen concentration. D. Degree of ocean anoxia. E. Relative atmospheric carbon dioxide concentration. F. Relative ocean sulfate concentration. G. Calculated $\delta^{13}C$ of new carbonate. H. Calculated seawater $\delta^{34}S$.*

Supplementary information 3: full COPSE model equations.

Below are the details of the modified COPSE model used in this work. Aside from the additions noted in the methods section, these details replicate those in Lenton et al. (2017). Figure S5 shows the model schematic, tables ST1-ST6 show model equations and parameters. Equations altered for this work are denoted by asterisks. Note that fluxes in the manuscript are denoted ‘F’ for better readability in that context, but fluxes in the model description drop the F to allow longer and more complex names, and to follow the code.

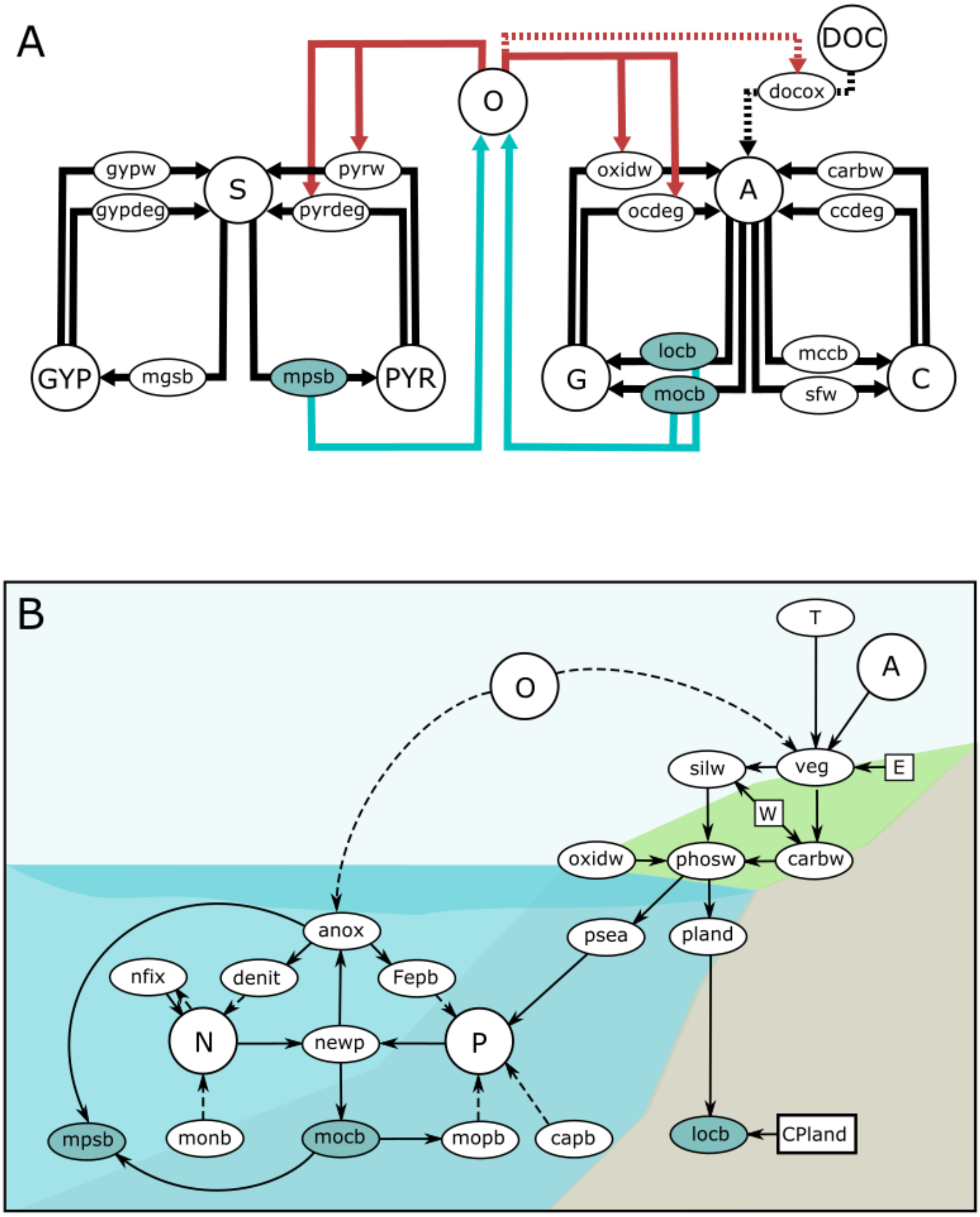

Figure S6. COPSE model schematic: *(A) Carbon, Sulphur and Oxygen cycle fluxes. Here arrows show mass fluxes, blue arrows show oxygen sources and red arrows show oxygen sinks. Dashed lines show DOC reservoir fluxes added for this work. (B) Dynamic nutrient and biosphere system. Here arrows show positive/direct (solid) or negative/inverse (dashed) relationships between model parameters. In both diagrams blue ovals show burial fluxes of organic carbon and pyrite sulphur, which are the long term sources of free oxygen.*

Table ST1. Core COPSE model reservoirs and differential equations.

Reservoir	Label	Differential equation	Initial size (mol)
Ocean (reactive) nitrogen	***N***	$\frac{d\boldsymbol{N}}{dt} = nfix - denit - monb$	4.35×10^{16}
Ocean (phosphate) phosphorus	***P***	$\frac{d\boldsymbol{P}}{dt} = psea - mopb - fepb - capb + \frac{DOCox}{CP_{DOC}}$	3.1×10^{15}
Atmosphere-ocean O_2	***O***	$\frac{d\boldsymbol{O}}{dt} = locb + mocb - oxidw - ocdeg + 2 \cdot mpsb - 2 \cdot pyrw - 2 \cdot pyrdeg - DOCox$	3.7×10^{19}
Atmosphere-ocean CO_2	***A***	$\frac{d\boldsymbol{A}}{dt} = oxidw + ocdeg + carbw + ccdeg - locb - mocb - mccb - sfw + DOCox$	3.193×10^{18}
Sedimentary organic (reduced) carbon	***G***	$\frac{d\boldsymbol{G}}{dt} = locb + mocb - oxidw - ocdeg$	1.25×10^{21}

Sedimentary carbonate (oxidised) carbon	***C***	$\frac{d\boldsymbol{C}}{dt} = mccb - carbw - ccdeg$	5.0x10[21]
Ocean (sulphate) sulphur	***S***	$\frac{d\boldsymbol{S}}{dt} = gypw + pyrw + gypdeg + pyrdeg - mgsb - mpsb$	4.0x10[19]
Sedimentary pyrite (reduced) sulphur	***PYR***	$\frac{d\boldsymbol{PYR}}{dt} = mpsb - pyrw - pyrdeg$	1.8x10[20]
Sedimentary gypsum (oxidised) sulphur	***GYP***	$\frac{d\boldsymbol{GYP}}{dt} = mgsb - gypw - gypdeg$	2.0x10[20]
Deep ocean DOC*	***DOC***	$\frac{d\boldsymbol{DOC}}{dt} = -DOCox$	$20 \times A_0$, $30 \times A_0$

Table ST2. Isotope calculations.

These quantities track the isotopic composition of the surface sulfur and carbon reservoirs.

Atmosphere and ocean carbon	$\frac{\boldsymbol{d(A \cdot \delta A)}}{\boldsymbol{dt}} = oxidw \cdot \delta_G + ocdeg \cdot \delta_G + carbw \cdot \delta_C + ccdeg \cdot \delta_G - locb(\delta_A - \Delta B) - mocb(\delta_A - \Delta B) - mccb \cdot \delta_A - sfw \cdot \delta_A + DOCox \cdot \delta_{DOC}$
Ocean sufate	$\frac{\boldsymbol{d(S \cdot \delta S)}}{\boldsymbol{dt}} = gypw \cdot \delta_{GYP} + pyrw \cdot \delta_{PYR} + gypdeg \cdot \delta_{GYP} + pyrdeg \cdot \delta_{PYR} - mgsb \cdot \delta_S - mpsb(\delta_S - \Delta S)$

Table ST3. Baseline values.

Process	**Label**	**Constant**	**Value** (mol/yr)
Nitrogen cycle			

Nitrogen fixation	*nfix*	k_3	8.67
Denitrification	*denit*	$2k_4$	8.6
Marine organic N burial	*monb*	k_2/CN_{sea}	0.07
Phosphorus cycle			
Reactive P weathering	*phosw*	k_{10}	42.5
Terrestrial organic P burial	*pland*	$k_{11}k_{10}$	2.5
Reactive P to ocean	*psea*	$(1-k_{11})k_{10}$	40
Marine organic P burial	*mopb*	k_2/CP_{sea}	10
Iron-sorbed (Fe-P) burial	*fepb*	k_6	10
Ca-bound (Ca-P) burial	*capb*	k_7	20
Carbon cycle (inorganic)			
Carbonate C degassing	*ccdeg*	k_{12}	15
Carbonate weathering	*carbw*	k_{14}	8
Silicate weathering	*silw*	k_{silw}	12
Granite weathering	*granw*	k_{granw}	9
Basalt weathering	*basw*	k_{basw}	3
Seafloor weathering	*sfw*	k_{sfw}	3
Carbonate burial	*mccb*	$k_{14}+k_{silw}$	20
Carbon cycle (organic)			
Organic C degassing	*ocdeg*	k_{13}	1.25
Oxidative C weathering	*oxidw*	k_{17}	3.75
Marine organic C burial	*mocb*	k_2	2.5
Terrestrial organic C burial	*locb*	k_5	2.5
Sulphur cycle			
Gypsum degassing	*gypdeg*	k_{gypdeg}	0.5
Pyrite degassing	*pyrdeg*	k_{pyrdeg}	0.25
Gypsum weathering*	*gypw*	k_{22}	1.0
Pyrite weathering	*pyrw*	k_{21}	0.45

Gypsum burial*	*mgsb*	k_{mgsb}	1.5
Pyrite burial	*mpsb*	k_{mpsb}	0.7

Table ST4. Model forcing factors. *(All normalised to 1 at present with the exception of insolation.)*

Note that all forcings are set to their starting early Phanerozoic values for the 'Ediacaran' state explored here. This includes setting all land-plant-related forcings to zero.

Forcing	Description	Basis	Source(s)
I	Insolation (solar luminosity)	Stellar physics	(Caldeira and Kasting, 1992)
D	Metamorphic and volcanic degassing	Inversion of sea level curve	(Mills et al., 2017)
U	Tectonic uplift	Sediment accumulation rates	((Berner, 2006; Ronov, 1993)
E	Plant evolution and land colonisation	Fossil record and model estimates of global net primary productivity	(Lenton et al., 2016), updated here
W	Plant enhancement of weathering	Experimental and field study results	(Lenton et al., 2012), updated here
CP_{land}	C/P burial ratio of terrestrial plant material	Attempt to capture Paleozoic coal deposition	(Lenton et al., 2016), updated here
B	Apportioning of carbonate burial between shallow and deep seas	Fossil record of evolution of planktonic calicifiers	(Berner, 1994)
a_{bas}	Exposed area of volcanic silicate rocks	Reconstructed area of large igneous provinces (LIPs) and volcanic islands	(Ernst, 2014; Mills et al., 2014)
a_{gran}	Kinetically-weighted area of non-volcanic silicate rocks	Reconstructed lithology of shield, shale, coal, evaporite	(Bluth and Kump, 1991)
PG	Paleogeography effect on runoff/weathering	Climate model simulations	(Royer et al., 2014)
b_{coal}	Depositional area of coal basins	Coal abundance data	(Bartdorff et al., 2008)
F	Selective biotic weathering of P relative to host rocks	Experimental results	(Lenton et al., 2016, 2012)

c_{cal}	Ocean calcium concentration	Best fit to fluid inclusion data	(Horita et al., 2002)
$\boldsymbol{S_{input}}$*	Sulfate input pulse	Exploring this hypothesis	This work; Wortmann and Paytan, 2012)

Table ST5. COPSE model functional forms
Units are mol/yr unless otherwise stated

$CO_2 = \boldsymbol{a}^2$	PAL
$\Delta T = k_c \cdot \ln CO_2 - k_l \cdot t/570$	K
$ignit = min(max(48 \cdot mO_2 - 9.08, 0), 5)$	No units
$V_{npp} = k_{npp} \cdot E \cdot (1.5 - 0.5 \cdot \boldsymbol{o}) \cdot \left(1 - \left(\frac{T-25}{25}\right)^2\right) \cdot \left(\frac{pCO_2 - P_{min}}{P_{1/2} + pCO_2 - P_{min}}\right)$	Relative
$mO_2 = \frac{\boldsymbol{o}}{\boldsymbol{o} + k_{16}}$	Atmospheres
$V = V_{npp} \cdot \frac{k_{fire}}{k_{fire} - 1 + ignit}$	Relative
$f_{biota} = \left[(1 - \min(V \cdot W, 1)) \cdot k_{15} \cdot {CO_2}^{0.5} + V \cdot W\right]$	Relative
$f_{runoff} = [1 + 0.038\Delta T]^{0.65}$	Relative
$g_{runoff} = 1 + 0.087\Delta T$	Relative
$f_T^i = e^{k_T^i \Delta T}$	Relative
$granw = k_{granw} \cdot U \cdot PG \cdot a_{gran} \cdot f_{Tgran} \cdot f_{runoff} \cdot f_{biota}$	
$basw = k_{basw} \cdot PG \cdot a_{bas} \cdot f_{Tbas} \cdot f_{runoff} \cdot f_{biota}$	
$silw = granw + basw$	
$carbw = k_{14} \cdot \boldsymbol{C} \cdot U \cdot PG \cdot g_{runoff} \cdot f_{biota}$	
gypw*$= k_{gypw} \cdot g_{runoff} + k_{gyp} \cdot g_{runoff} \cdot S_{input}$	
pyrw*$= k_{pyrw} \cdot g_{runoff} + k_{pyr} \cdot g_{runoff} \cdot S_{input}$	
$sfw = k_{sfw} \cdot D \cdot e^{k_T^{sfw} \Delta T}$	
$oxidw = k_{17} \cdot U \cdot \boldsymbol{g} \cdot \boldsymbol{o}^{0.5} \cdot g_T$	

$phosw = k_{10} \cdot F \cdot \left(k_{Psilw} \cdot \frac{silw}{k_{silw}} + k_{Pcarbw} \cdot \frac{carbw}{k_{14}} + k_{Poxidw} \cdot \frac{oxidw}{k_{17}}\right)$	
$pland = k_{11} \cdot V \cdot phosw \cdot \left(k_{aq} + \left(1 - k_{aq}\right) \cdot b_{coal}\right)$	
$locb = \left(\frac{C}{P}\right)_{land} \cdot pland = k_5 \cdot CP_{land} \cdot pland'$	
$psea = phosw - pland$	
$newp = r_{C:P} \cdot min(30.9 \cdot \boldsymbol{n}/r_{N:P}, 2.2 \cdot \boldsymbol{p})$	
$anox = \frac{1}{1 + e^{-k_{anox}(k_u \cdot newp\prime - \boldsymbol{o})}}$	Fraction of seafloor
$denit = k_4 \left(1 + \frac{anox}{1 - k_1}\right) \cdot \boldsymbol{n}$	
$nfix = k_3 \left(\frac{\boldsymbol{P} - \boldsymbol{N}/r_{N:P}}{P_0 - N_0/r_{N:P}}\right)^2$ for $\frac{\boldsymbol{N}}{r_{N:P}} < \boldsymbol{P}$, else 0	
$monb = mocb/CN_{sea}$	
$mocb = k_2 \cdot (newp')^2$	
$mopb = mocb/CP_{sea}$	
$CP_{sea} = \frac{k_{oxic} \cdot k_{anoxic}}{(1 - anox) \cdot k_{anoxic} + anox \cdot k_{oxic}}$	C:P ratio
$fepb = \frac{k_6}{k_1} \cdot (1 - anox) \cdot \boldsymbol{p}$	
$capb = k_7 \cdot newp'^2 \cdot f(anox)$	
$\boldsymbol{mpsb}^* = k_{mpsb} \cdot \frac{1}{\boldsymbol{o}} \cdot \boldsymbol{S} \cdot mocb' \ + \ pyfrac \cdot (pyrw_{pulse} + gypw_{pulse})$	
$\boldsymbol{mgsb}^* = k_{mgsb} \cdot \boldsymbol{0.5} + (1 - pyfrac) \cdot (pyrw_{pulse} + gypw_{pulse})$	
$mccb = silw + carbw$	
$gypdeg = k_{gypdeg} \cdot D \cdot \boldsymbol{gyp}$	
$pyrdeg = k_{pyrdeg} \cdot D \cdot \boldsymbol{pyr}$	
$ccdeg = k_{12} \cdot D \cdot B \cdot \boldsymbol{c}$	
$ocdeg = k_{13} \cdot D \cdot \boldsymbol{g}$	
$\boldsymbol{DOCox}^* = \begin{cases} 0\,, & DOC < 1 \times 10^{12}\ mol \\ -\frac{k}{1 + e^{-a(1 - ANOX - c)}} \left(\frac{DOC}{DOC_0}\right), & DOC \geq 1 \times 10^{12}\ mol \end{cases}$	

Table ST6. COPSE model non-flux parameters.

Label	**Meaning**	**Default value**
k_1	Present ocean oxic fraction	0.997527
k_{15}	Pre-plant weathering	0.15
k_{fire}	Fire frequency control	3
k_c	Climate sensitivity control	4.328°C
k_l	Luminosity sensitivity control	7.4°C
k_T^{sfw}	Temperature sensitivity of seafloor weathering	0.0608
k_T^{gran}	Temperature sensitivity of granite weathering	0.0724
k_T^{bas}	Temperature sensitivity of basalt weathering	0.0608
k_{Psilw}	Silicates fraction of P weathering	0.8
k_{Pcarbw}	Carbonates fraction of P weathering	0.14
k_{Poxidw}	Oxidative fraction of P weathering	0.06
k_{aq}	Terrestrial organic matter burial fraction in aquatic settings	0.8
$\boldsymbol{k_u}^*$	Nutrient utilisation efficiency	0.4
$\boldsymbol{k_{anox}}^*$	Sharpness of oxic-anoxic transition	10

Supplementary Information 4: Geological record of Tonian evaporite sulfate deposits and their erosion during middle Ediacaran time

The Tonian Period witnessed the largest evaporite depositional event of pre-Ediacaran time during the break-up of the Rodinia supercontinent (Evans, 2006). Estimates for the current preserved volume of Tonian evaporites range from 375,000 km^3 (Evans, 2006) to 912,400 km^3 (Prince et al., 2019) and place Tonian deposits (ca. 830 – ca. 770 Ma) among the largest basin-scale evaporite deposits in the world. As outlined further below, later erosional events mean that initial volumes would have been substantially higher. The high calcium sulfate content of these evaporite deposits (Prince et al., 2019; Schmid, 2017; Turner and Bekker, 2016) and relatively unchanging seawater $\delta^{34}S$ values (Prince et al., 2019; Strauss, 1993) are consistent with the build-up of a large marine sulfate reservoir during the early Neoproterozoic (Fakhraee et al., 2019).

Because evaporite basins are restricted geographically, their emergence and erosion depend on regional tectonic events. Fold belts preserving relicts of major Tonian evaporite basins are consistent with initial inversion and weathering in middle to early late Ediacaran time. Their geographic situations, in some cases, suggest proximity to areas of high productivity, consistent with anoxia and pyrite burial. However, it is entirely plausible that areas of evaporite weathering (high sulfate input) and pyrite burial (high sulfide output) were geographically separate, as the latter would be more closely related to locally high nutrient input, either through chemical weathering or upwelling. Area estimates below in brackets derive from Prince et al (2019).

Centralian Superbasin, Australia (*683,000 km³*). The largest preserved Tonian basin-scale evaporite deposit, that of Australia's Centralian Superbasin (Browne and Bitter Springs formations and correlatives), was deposited at 20 ± 5° palaeolatitude (with normalised preserved area factor of ***2.8x*** (Evans, 2006) in an intracontinental sag or else continent-scale re-entrant (Li and Evans, 2011). Stratigraphic coherence of the Centralian Superbasin (Walter et al., 1995) or at least persistence of accommodation space (Camacho et al., 2015) continues into Ediacaran time when local unconformities (e.g., between lower and upper Arumbera Formation; beneath Table Hill Formation; and above the

Rodda beds) express tectonic effects of the 650-550 Ma Paterson-Petermann Orogen, across which northern and southern Australian subcratons shortened by 100's km (Bagas, 2004). Preserved Centralian strata are truncated locally after the Shuram-Wonoka-DOUNCE carbon isotopic excursion had begun in Boondawari Formation and metamorphosed elsewhere by 560 Ma and thickened transpressionally by 550 Ma (Camacho and Mcdougal, 2000). It is reasonable to extrapolate that regional exhumation and tectonic erosion of the Centralian Superbasin had begun no later than ~10 million years earlier, ~570 Ma (i.e., ~cm/yr rate-of-collision extrapolated to ~100 km shortening).

At that time, applying Bunyeroo-Wonoka palaeomagnetic poles (Williams and Schmidt, 2018), weathered Centralian evaporite would have washed southward into an equator-facing, northern margin of a "Kuunga embayment" of the meridional, proto-East Gondwanaland margin. This Panthalassa-facing, trans-equatorial embayment to a high-relief, western continental boundary swathe would have been an expected site for subtropical upwelling, high primary productivity, and tropical stagnation in the near ocean basin.

Amundsen and Mackenzie-Ogilvie basins, Canada (*193,000 km^2*). The next largest preserved deposit (norm'd area ***1.8x***), e.g. Minto Inlet Formation (Evans, 2006) or Ten Stone Formation (Turner and Bekker, 2015), extends across both Amundsen Basin and Mackenzie-Ogilvie Basin of NW Canada and was deposited at 20 ± 5° along aulocogens of the rifting NW Laurentian margin (Prince et al., 2019). While accommodation probably was enabled by post-rift sag, the region was always low-relief, receiving mostly distal siliciclastic debris from the Grenville Orogen (Rainbird et al., 2012). A low-amplitude, Ediacaran-age Mackenzie Arch inverted part of these depocentres, particularly in the modern Mackenzie Valley. Time-transgressive onlap of Ediacara-bearing siliciclastics atop a post-632 Ma, earliest Ediacaran exposure surface indicates that most exhumation occurred ca. 572-565 Ma though persisting locally into the Cambrian (MacLean et al., 2014), adopting early Ediacaran ages (Pu et al., 2016).

At that time, applying the Johnnie Fm pole (Gillett and Van Alstine, 1979), Minto Inlet-Mackenzie Arch evaporite would have washed northward into the offshore of a zonal, equatorial passive margin facing expansive ocean poleward. This equatorial position along a straight, zonal margin would have been an expected site for periodic anoxia associated with temperature-driven dysoxia and shallow-level return flow of the broader thermohaline circulation.

Adelaide fold belt, South Australia (*100,000 km^2*). Smaller preserved Tonian evaporites in the Adelaide Rift Complex of South Australia (norm'd preserved area ***1.5x*** [Evans, 2006]) were deposited at subtropical latitude. Salt tectonics are evident throughout Cryogenian and into Ediacaran time (Preiss, 2000), presumably responding to buoyancy of attenuated crust throughout a wide, actively-rifting plate boundary zone inheriting complex architecture from Archean through Mesoproterozoic tectonic domain-bounding structures. Because the steeply-dipping, volcanic margin was established and drift phase begun along the Tasman line no earlier than 586-575 Ma (Calver et al., 2004; Meffre et al., 2004), exhumation along a continental raised rift shoulder and potential erosion of exposed salt diapirs is reasonably estimated as mid-Ediacaran age.

At that time, applying published Bunyeroo-Wonoka palaeomagnetic poles (Williams and Schmidt, 2018), weathered Adelaide Rift Complex evaporite would have washed south-eastward across a storm-dominated, Wonoka carbonate platform (Haines, 1988) along structural inlets at subtropical latitude. The character of the deep ocean basins offshore the volcanic rifted margin of south-eastern Australia seem more speculative than that of the margins offshore Centralian and Minto Inlet Tonian evaporites.

Duruchaus basin, Namibia (*30,000 km^2*). Contiguous correlatives of minor playa-setting evaporite of the Duruchaus Formation in the Gariep-Kaoko belt of Namibia (norm'd preserved area ***0.3x*** [Evans, 2006]) would have been inverted and eroded starting ~575 Ma, when subduction began along the Damaride margin of Congo craton (Frimmel and Frank, 1998). Such erosion probably ended by ca. 545 Ma (ibid.), when the foreland basins were established after oceanic terranes accreted, although collision with Kalahari craton continued in the Gariep belt throughout the Cambrian (Gray et al., 2008).

Through the last half of the Ediacaran Period, weathered Duruchaus evaporite would have washed into archipelagos of the Adamastor-Khomas oceans, conventionally placed at temperate southern palaeolatitudes although no direct or straightforward applied palaeomagnetic constraints are applicable.

Aside from the spatially restricted character of these ocean basins with convolute passages and bays between high-relief cratonic margins, other aspects affecting potential pyrite burial must remain speculative.

Central African copperbelt (*50,000 km^2*). Tonian evaporite of the Zambian-Congolese Copperbelt (normalised preserved area ***0.5x*** (Evans, 2006)) also was exhumed in middle to late Ediacaran time: probably <573 Ma, the age of a detrital zircon in the foreland Fungurume Group, which unconformably overlies earlier Ediacaran siliciclastics, *cf.* (Master and Wendorff, 2011). This age is consistent with the age of extensive anorogenic Hook batholith intrusion in Zambia and probably intrusion of mantle-derived mafic plutons in the "domes" belt of the Zambian-Congolese border zone; both should have driven regional exhumation of Copperbelt rift-fill. However, it must be noted that major collision and inversion of the Lufilian arc, which certainly included salt diapirism and exploitation of Tonian evaporite by thrust faults in the Congolese foreland, was an entirely Cambrian event which persisted to the Cambrian-Ordovician boundary.

The palaeolatitude and character of the Zambezi-Mozambique belt ocean basins into which Copperbelt evaporites would have washed is speculative.

Considered altogether, every major Tonian evaporite deposit was tectonically exhumed during middle to late Ediacaran time; mostly after ca. 570 Ma. This is a remarkable coincidence since the geodynamic settings of these deformation events were diverse. Centralian evaporites were exhumed by transpressional orogenesis and intraplate deformation at the edge of the Kuunga Orogen; Amundsen-Mackenzie-Ogilvie evaporites were exhumed by cryptic rejuvenation of a long-lived basement structure on a passive margin; South Australian evaporites were exhumed sympathetic to development of a raised volcanic rift margin; Duruchaus was exhumed by early Damaride accretion of terranes onto an active margin; and the Copperbelt was exhumed by intrusion of an anorogenic large igneous province.

References

Algeo, T.J., Luo, G.M., Song, H.Y., Lyons, T.W., Canfield, D.E., 2015. Reconstruction of secular variation in seawater sulfate concentrations. Biogeosciences. https://doi.org/10.5194/bg-12-2131-2015

Bagas, L., 2004. Proterozoic evolution and tectonic setting of the northwest Paterson Orogen, Western Australia. Precambrian Res. https://doi.org/10.1016/j.precamres.2003.09.011

Bartdorff, O., Wallmann, K., Latif, M., Semenov, V., 2008. Phanerozoic evolution of atmospheric methane. Global Biogeochem. Cycles. https://doi.org/10.1029/2007GB002985

Berner, R.A., 2006. Inclusion of the weathering of volcanic rocks in the GEOCARBSULF model. Am. J. Sci. https://doi.org/10.2475/05.2006.01

Berner, R.A., 1994. GEOCARB II: a revised model of atmospheric CO2over Phanerozoic time. Am. J. Sci. https://doi.org/10.2475/ajs.294.1.56

Bluth, G.J.S., Kump, L.R., 1991. Phanerozoic paleogeology. Am. J. Sci. https://doi.org/10.2475/ajs.291.3.284

Caldeira, K., Kasting, J.F., 1992. The life span of the biosphere revisited. Nature. https://doi.org/10.1038/360721a0

Calver, C.R., Black, L.P., Everard, J.L., Seymour, D.B., 2004. U-Pb zircon age constraints on late Neoproterozoic glaciation in Tasmania. Geology. https://doi.org/10.1130/G20713.1

Camacho, A., Armstrong, R., Davis, D.W., Bekker, A., 2015. Early history of the Amadeus Basin: Implications for the existence and geometry of the Centralian Superbasin. Precambrian Res. https://doi.org/10.1016/j.precamres.2014.12.004

Camacho, A., Mcdougal, I., 2000. Intracratonic, strike-slip partitioned transpression and the formation and exhumation of eclogite facies rocks: An example from the Musgrave Block, central Australia. Tectonics. https://doi.org/10.1029/1999TC001151

Canfield, D.E., Farquhar, J., 2009. Animal evolution, bioturbation, and the sulfate concentration of the oceans. Proc. Natl. Acad. Sci. U. S. A. 106, 8123–8127. https://doi.org/10.1073/pnas.0902037106

Chen, X., Ling, H.-F., Vance, D., Shields-Zhou, G.A., Zhu, M., Poulton, S.W., Och, L.M., Jiang, S.-Y., Li, D., Cremonese, L., Archer, C., 2015. Rise to modern levels of ocean oxygenation coincided with the Cambrian radiation of animals. Nat. Commun. 6, 1–7. https://doi.org/10.1038/ncomms8142

Crockford, P.W., Kunzmann, M., Bekker, A., Hayles, J., Bao, H., Halverson, G.P., Peng, Y., Bui, T.H., Cox, G.M., Gibson, T.M., Wörndle, S., Rainbird, R., Lepland, A., Swanson-Hysell, N.L., Master, S., Sreenivas, B., Kuznetsov, A., Krupenik, V., Wing, B.A., 2019. Claypool continued: Extending the isotopic record of sedimentary sulfate. Chem. Geol. https://doi.org/10.1016/j.chemgeo.2019.02.030

Ernst, R.E., 2014. Large igneous provinces, Large Igneous Provinces. https://doi.org/10.1017/CBO9781139025300

Evans, D.A.D., 2006. Proterozoic low orbital obliquity and axial-dipolar geomagnetic field from evaporite palaeolatitudes. Nature. https://doi.org/10.1038/nature05203

Fakhraee, M., Hancisse, O., Canfield, D.E., Crowe, S.A., Katsev, S., 2019. Proterozoic seawater sulfate scarcity and the evolution of ocean–atmosphere chemistry. Nat. Geosci. https://doi.org/10.1038/s41561-019-0351-5

Fike, D.A., Grotzinger, J.P., Pratt, L.M., Summons, R.E., 2006. Multi-stage Ediacaran ocean oxidation and its impact on evolutionary radiation. Geochim. Cosmochim. Acta 70, A173.

Frimmel, H.E., Frank, W., 1998. Neoproterozoic tectono-thermal evolution of the Gariep Belt and its basement, Namibia and South Africa. Precambrian Res. https://doi.org/10.1016/S0301-9268(98)00029-1

Gillett, S.L., Van Alstine, D.R., 1979. Paleomagnetism of Lower and Middle Cambrian sedimentary rocks from the Desert Range, Nevada. J. Geophys. Res. https://doi.org/10.1029/JB084iB09p04475

Gray, D.R., Foster, D.A., Meert, J.G., Goscombe, B.D., Armstrong, R., Trouw, R.A.J., Passchier, C.W., 2008. A Damara orogen perspective on the assembly of southwestern Gondwana. Geol. Soc. London, Spec. Publ. https://doi.org/10.1144/SP294.14

Haines, P.W., 1988. Storm-dominated mixed carbonate / siliciclastic shelf sequence displaying cycles of hummocky cross-stratification, late Proterozoic Wonoka Formation, South Australia. Sediment. Geol. https://doi.org/10.1016/0037-0738(88)90071-1

Horita, J., Zimmermann, H., Holland, H.D., 2002. Chemical evolution of seawater during the Phanerozoic: Implications from the record of marine evaporites. Geochim. Cosmochim. Acta. https://doi.org/10.1016/S0016-7037(01)00884-5

Lenton, T.M., Crouch, M., Johnson, M., Pires, N., Dolan, L., 2012. First plants cooled the Ordovician. Nat. Geosci. https://doi.org/10.1038/ngeo1390

Lenton, T.M., Dahl, T.W., Daines, S.J., Mills, B.J.W., Ozaki, K., Saltzman, M.R., Porada, P., 2016. Earliest land plants created modern levels of atmospheric oxygen. Proc. Natl. Acad. Sci. 113, 9704–9709. https://doi.org/10.1073/pnas.1604787113

Lenton, T.M., Daines, S.J., Mills, B.J.W., 2017. COPSE reloaded: An improved model of biogeochemical cycling over Phanerozoic time. Earth-Science Rev. 178, 1–28. https://doi.org/10.1016/j.earscirev.2017.12.004

Li, Z.X., Evans, D.A.D., 2011. Late Neoproterozoic 40° intraplate rotation within Australia allows for a tighter-fitting and longer-lasting Rodinia. Geology. https://doi.org/10.1130/G31461.1

MacLean, B.C., Fallas, K.M., Hadlari, T., 2014. The multi-phase Keele Arch, central Mackenzie Corridor, Northwest Territories. Bull. Can. Pet. Geol. https://doi.org/10.2113/gscpgbull.62.2.68

Master, S., Wendorff, M., 2011. Chapter 12 Neoproterozoic glaciogenic diamictites of the Katanga Supergroup, Central Africa. Geol. Soc. London, Mem. https://doi.org/10.1144/m36.12

Meffre, S., Direen, N.G., Crawford, A.J., Kamenetsky, V., 2004. Mafic volcanic rocks on King Island, Tasmania: Evidence for 579 Ma break-up in east Gondwana. Precambrian Res. https://doi.org/10.1016/j.precamres.2004.08.004

Mills, B., Daines, S.J., Lenton, T.M., 2014. Changing tectonic controls on the long-term carbon cycle from Mesozoic to present. Geochemistry, Geophys. Geosystems 15, 4866–4884. https://doi.org/10.1002/2014GC005530

Mills, B.J.W., Scotese, C.R., Walding, N.G., Shields, G.A., Lenton, T.M., 2017. Elevated CO_2 degassing rates prevented the return of Snowball Earth during the Phanerozoic. Nat. Commun. 8, 1–7. https://doi.org/10.1038/s41467-017-01456-w

Preiss, W. V., 2000. The Adelaide Geosyncline of South Australia and its significance in Neoproterozoic continental reconstruction. Precambrian Res. 100, 21–63. https://doi.org/10.1016/S0301-9268(99)00068-6

Prince, J.K.G., Rainbird, R.H., Wing, B.A., 2019. Evaporite deposition in the mid-Neoproterozoic as a driver for changes in seawater chemistry and the biogeochemical cycle of sulfur. Geology. https://doi.org/10.1130/g45464.1

Pu, J.P., Bowring, S.A., Ramezani, J., Myrow, P., Raub, T.D., Landing, E., Mills, A., Hodgin, E., Macdonald, F.A., 2016. Dodging snowballs: Geochronology of the Gaskiers glaciation and the first appearance of the Ediacaran biota. Geology. https://doi.org/10.1130/G38284.1

Rainbird, R., Cawood, P., Gehrels, G., 2012. The Great Grenvillian Sedimentation Episode: Record of Supercontinent Rodinia's assembly, in: Tectonics of Sedimentary Basins: Recent Advances. https://doi.org/10.1002/9781444347166.ch29

Ronov, A.B., 1993. Stratisfera-Ili Osadochnaya Obolochka Zemli (Kolichestvennoe Issledovanie). Nauka, Moskva.

Royer, D.L., Donnadieu, Y., Park, J., Kowalczyk, J., Goddéris, Y., 2014. Error analysis of CO_2 and O_2 estimates from the long-term geochemical model GEOCARBSULF. Am. J. Sci. https://doi.org/10.2475/09.2014.01

Saltzman, M.R., Thomas, E., 2012. Chapter 11 - Carbon Isotope Stratigraphy, in: The Geologic Time Scale. pp. 207–232. https://doi.org/http://dx.doi.org/10.1016/B978-0-444-59425-9.00011-1

Schmid, S., 2017. Neoproterozoic evaporites and their role in carbon isotope chemostratigraphy

(Amadeus Basin, Australia). Precambrian Res. 290, 16–31. https://doi.org/10.1016/j.precamres.2016.12.004

Strauss, H., 1993. The sulfur isotopic record of Precambrian sulfates: new data and a critical evaluation of the existing record. Precambrian Res. https://doi.org/10.1016/0301-9268(93)90035-Z

Turner, E.C., Bekker, A., 2016. Thick sulfate evaporite accumulations marking a mid-Neoproterozoic oxygenation event (Ten Stone Formation, Northwest territories, Canada). Bull. Geol. Soc. Am. https://doi.org/10.1130/B31268.1

Walter, M.R., Veevers, J.J., Calver, C.R., Grey, K., 1995. Neoproterozoic stratigraphy of the Centralian Superbasin, Australia. Precambrian Res. https://doi.org/10.1016/0301-9268(94)00077-5

Williams, G.E., Schmidt, P.W., 2018. Shuram–Wonoka carbon isotope excursion: Ediacaran revolution in the world ocean's meridional overturning circulation. Geosci. Front. https://doi.org/10.1016/j.gsf.2017.11.006

Wortmann, U.G., Paytan, A., 2012. Rapid variability of seawater chemistry over the past 130 million years. Science (80-.). 337, 334–336. https://doi.org/10.1126/science.1220656

Wu, N., Farquhar, J., Fike, D.A., 2015. Ediacaran sulfur cycle: Insights from sulfur isotope measurements ($\delta^{33}S$ and $\delta^{34}S$) on paired sulfate-pyrite in the Huqf Supergroup of Oman. Geochim. Cosmochim. Acta. https://doi.org/10.1016/j.gca.2015.05.031